Supplementary Information

Dual-Functional SnS_2-CuS Heterostructure for Zinc Anode Protection and Conversion-Type Anode Toward Advanced Aqueous Zinc-Ion Batteries

Shaoyan Huang [a], *Shuling Liu* [a, *], *Sha Fan* [b, c], *Rui Su* [a], *Deliang Tian* [b, c], Zili Deng [b, c], *Jinbao Li* [b, c, *], *Jianbo Tong* [a, *]

[a] Department of Chemistry and Chemical Engineering, Shaanxi Collaborative Innovation Center of Industrial Auxiliary Chemistry & Technology, Key Laboratory of Auxiliary Chemistry and Technology for Chemical Industry, Ministry of Education, The Youth Innovation Team of Shaanxi Universities, Shaanxi University of Science and Technology, Xi'an, Shaanxi, 710021, China

[b] College of Bioresources Chemical & Materials Engineering, Shaanxi University of Science & Technology, Xi'an, Shaanxi, 710021, China

[c] National Demonstration Center for Experimental Light Chemistry Engineering Education, Shaanxi Provincial Key Laboratory of Papermaking Technology and Specialty Paper Development, Xi'an, Shaanxi, 710021, China

[*]Corresponding author.

E-mail address: shulingliu@aliyun.com (Shuling Liu); lijinbao@sust.edu.cn (Jinbao Li); jianbotong@aliyun.com (Jianbo Tong)

Section 1 Experimental Methods

1.1. Synthesis of MnO_2

The synthesis of MnO_2 was carried out via a one-step hydrothermal method. Specifically, 12.5 mmol of potassium permanganate and 2 mmol of manganese sulfate monohydrate were sequentially dissolved in 80 mL of deionized water, followed by ultrasonication and vigorous stirring for 30 min to ensure complete dissolution and homogenization. The resulting solution was then transferred into a 100 mL autoclave lined with polytetrafluoroethylene and heated at 160 °C for 24 h. After natural cooling to room temperature, the precipitate was collected and thoroughly washed with ethanol and deionized water to remove residual ions. The purified product was dried at 80 °C for 12 h to yield the target MnO_2 material. To further eliminate potential impurities, the sample was subjected to thermal annealing under a nitrogen atmosphere at 350 °C for 3 h with a controlled heating rate of 5 °C/min.

1.2. Preparation of cathode materials

The as-prepared active material was thoroughly mixed with carbon black and polyvinylidene fluoride (PVDF) in a weight ratio of 7:2:1 using N-Methyl-2-pyrrolidone (NMP) solvent to obtain a homogeneous slurry. Subsequently, the slurry was evenly coated onto titanium foil and dried overnight at 80 °C under vacuum conditions. The dried electrodes were then punched into circular discs with a diameter of 12 mm, achieving an active material loading of approximately 0.6 mg cm^{-2}.

1.3. Preparation of anode materials

Anode fabrication for aqueous zinc-ion batteries (AZIBs): A homogeneous slurry was prepared by dispersing the synthesized SnS_2-CuS heterostructure and PVDF binder in NMP solvent at a mass ratio of 9:1, followed by thorough mixing. The resulting slurry was uniformly coated onto zinc foil using a doctor blade with a coating thickness of 20 μm and subsequently dried overnight at 80 °C under vacuum to ensure complete solvent removal. After drying, the electrode was punched into circular discs with a diameter of 12 mm for use as working anodes.

Anode fabrication for rocking-chair zinc-ion batteries (RCZIBs): A homogeneous slurry was prepared by dispersing the synthesized SnS_2-CuS heterostructure, carbon black conductive additive, and PVDF binder in NMP solvent at a mass ratio of 7:2:1, followed by thorough mixing to ensure uniformity. The resulting slurry was uniformly coated onto copper foil using a doctor blade, and the electrode was dried overnight under vacuum at 80 °C to completely remove residual solvent. After drying, the electrode was punched into circular discs with a diameter of 12 mm, with an active material loading of approximately 0.8 mg cm^{-2}.

1.4. Assembly of button batteries

The button batteries were assembled the air using CR2032 types, Whatman GF/A glass fiber filter paper as separators.

Symmetrical cell assembly: The symmetrical cells were assembled using zinc foils coated with SnS_2-CuS as both the cathode and anode, with 2 M $ZnSO_4$ aqueous solution serving as the electrolyte.

Half-cell assembly: The half-cell was constructed using a copper foil coated with the SnS_2-CuS heterostructure as the cathode and a zinc foil as the anode, with 2 M $ZnSO_4$ aqueous solution employed as the electrolyte.

Assembly of AZIBs full cells: The full cell was assembled using MnO_2 as the cathode and zinc foil modified with SnS_2-CuS heterostructure as the anode, with an aqueous electrolyte consisting of 2 M $ZnSO_4$ and 0.1 M $MnSO_4$.

Full-cell assembly of RCZIBs: The cell was assembled using MnO_2 as the cathode and SnS_2-CuS heterostructure as a zinc-free anode, with 2 M $ZnSO_4$ aqueous solution serving as the electrolyte.

1.5. DFT calculation method

The structural optimization and property calculations of the model are performed by the CASTEP module. The generalized gradient approximation (GGA) of the Perdew-Burke-Ernzerhof (PBE) function is used to describe the exchange-correlation potential. In the calculations, the cutoff energy of the plane wave basis set is 500 eV, the geometric structure was optimized until all the residual forces on each atom were smaller than 0.03 eV/Å. For the geometrical optimization setting, the total energy change and displacement were set to 1.0×10^{-5} eV and 0.001 Å, respectively.

The crystal surfaces of (010), and (002) were selected and a 2×2×1 supercell was performed.

20 Å vacuum space was designed to eliminate interactions between neighboring periodic layers of models.

Use TS method for DFT-D correction to enhance the description of the adsorbed system.

1.6. In-situ testing method

In-situ XRD measurements were performed on a Bruker D8 Advance diffractometer equipped with Cu Kα radiation at 40 kV and 40 mA. The diffraction patterns were collected over a 2θ range of 15-60° with a step size of 0.02° and a scanning speed of 2° min^{-1}. During the galvanostatic charge-discharge process, in-situ XRD tests were continuously conducted within the operating potential window to record the real-time phase evolution and crystal structure variation of the SnS_2-CuS electrode, revealing its reversible energy storage mechanism.

In-situ EIS was carried out on a CHI760E electrochemical workstation. The tests were performed at different charge/discharge equilibrium potentials with an AC amplitude of 5 mV over a frequency range from 0.01 Hz to 10^5 Hz. The real-time impedance variation of the SnS_2-CuS electrode during Zn^{2+} insertion and extraction was continuously monitored, so as to analyze the dynamic evolution of interfacial charge transfer and ion diffusion behavior.

Section 2 Supporting image

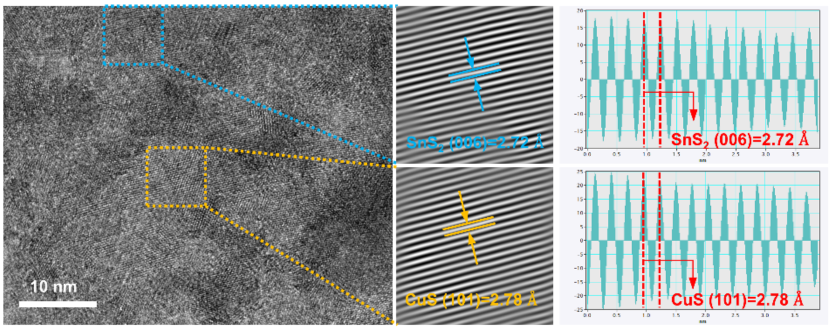

Fig. S1. HRTEM images and lattice parameters of SnS_2-CuS.

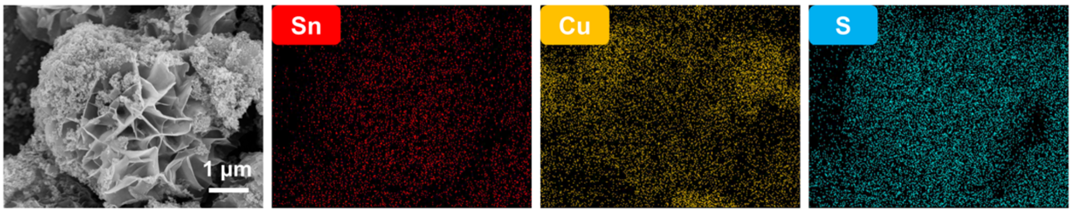

Fig. S2. SEM and EDS characterization results of the SnS_2-CuS heterostructure.

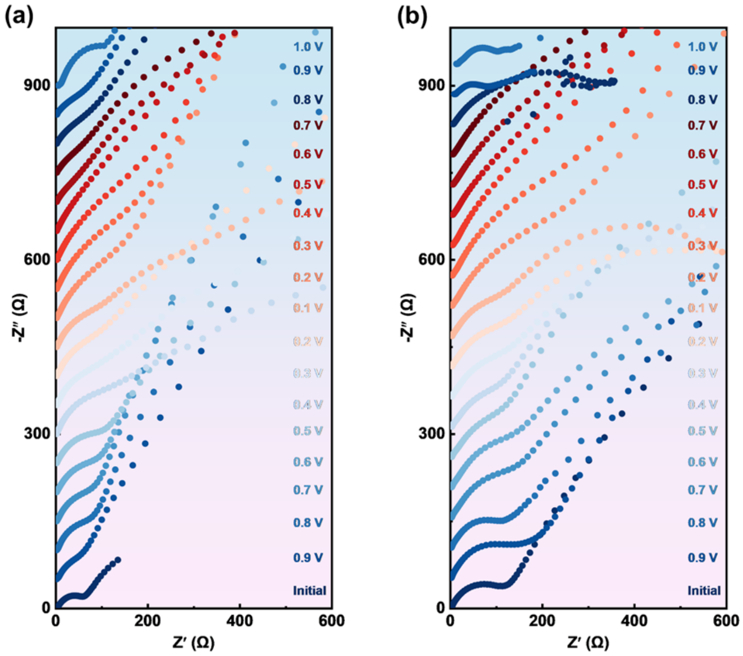

Fig. S3. In situ EIS analysis of zinc-copper half-cells with different cathodes: (a) CuS; (b) SnS_2.

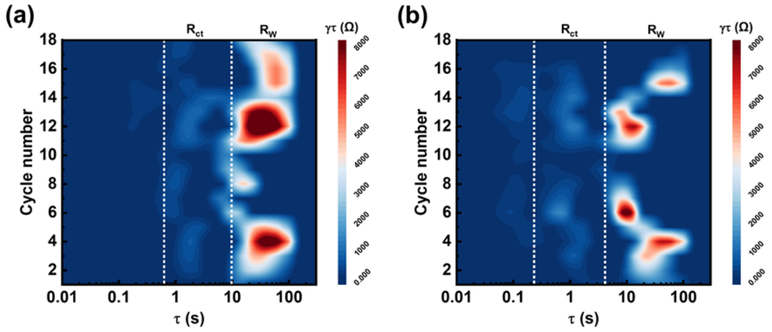

Fig. S4. DRT evolution of Zn-Cu half cells with different cathodes: (a) CuS; (b) SnS_2.

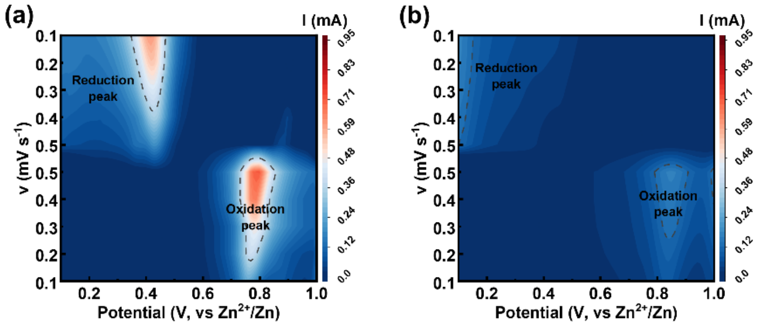

Fig. S5. Contour plots of CV curves for (a) CuS electrode; (b) SnS_2 electrode.

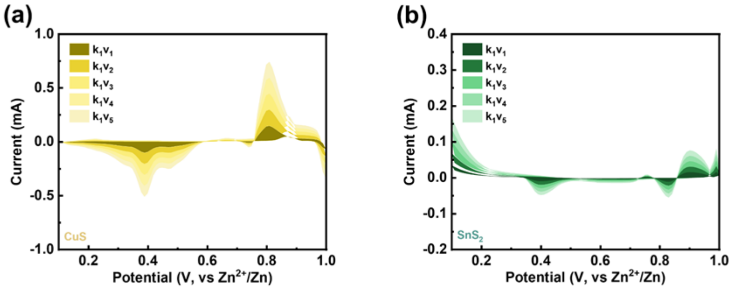

Fig. S6. Integral area of the pseudocapacitive contribution for different cathode zinc-copper half-cells: (a) CuS; (b) SnS_2.

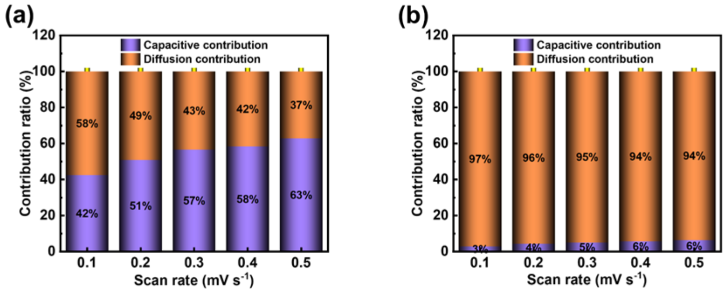

Fig. S7. Pseudocapacitive contribution ratio of different cathode zinc-copper half-cells at various scan rates: (a) CuS; (b) SnS_2.

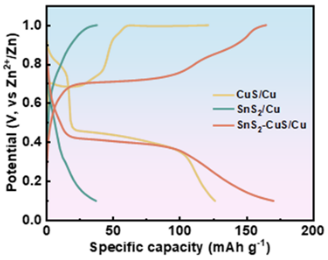

Fig. S8. The charging and discharging curves of different batteries.

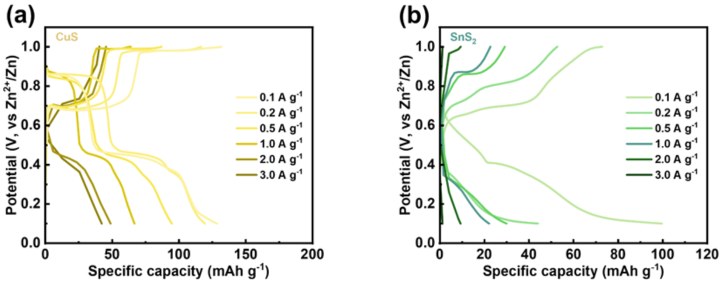

Fig. S9. Charge and discharge curves of different zinc-copper half-cells under rate capability testing: (a) CuS; (b) SnS_2.

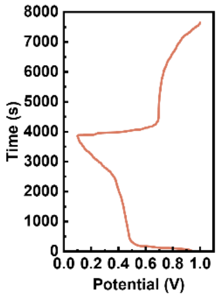

Fig. S10. Time-voltage curve corresponding to the in-situ XRD test.

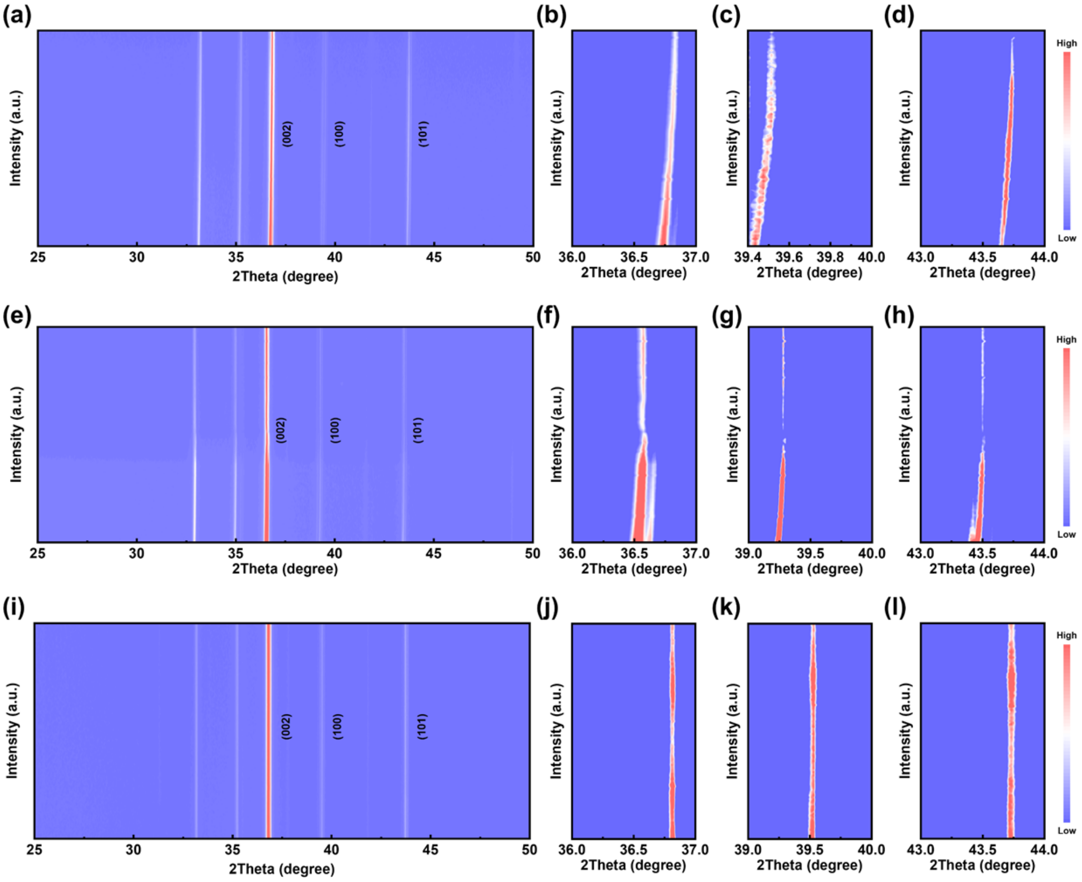

Fig. S11. In situ XRD analysis of zinc anodes in different zinc-copper half-cells: (a)-(d) CuS; (e)-(h) SnS_2; (i)-(l)SnS_2-CuS.

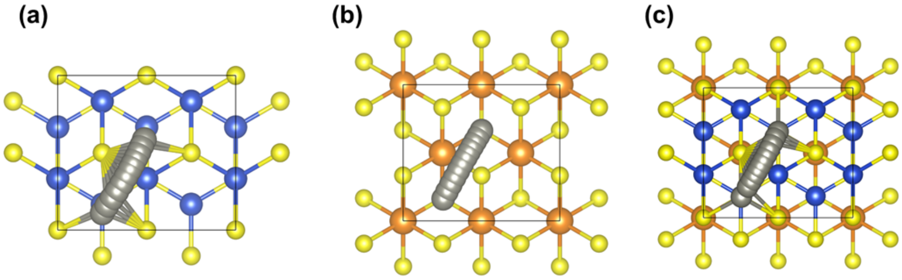

Fig. S12. Zinc ion diffusion paths.

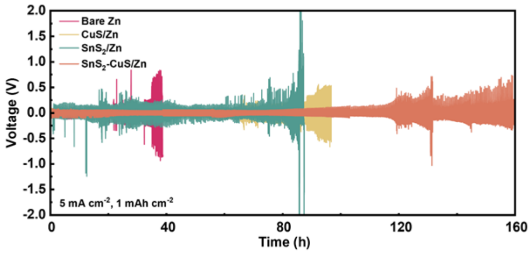

Fig. S13. Cycling voltage-time curves of symmetric cells assembled with different materials at 5 mA cm^{-2} and 1 mAh cm^{-2}.

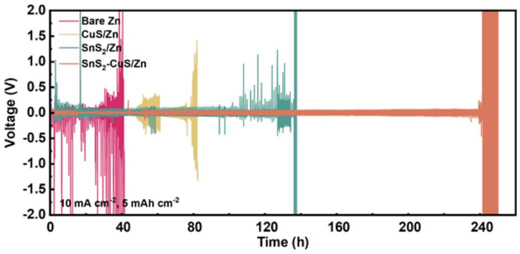

Fig. S14. Cycling voltage-time curves of symmetric cells assembled with different materials at 10 mA cm^{-2} and 5 mAh cm^{-2}.

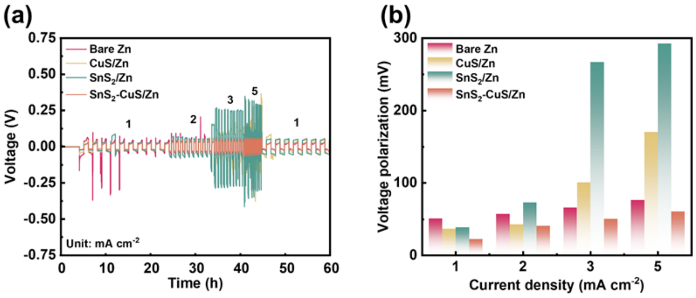

Fig. S15. (a) Rate performance and (b) overpotential of symmetric cells assembled with different materials.

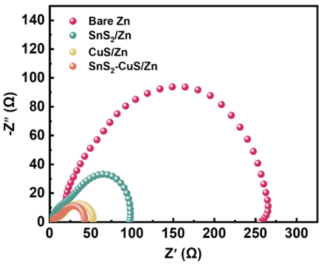

Fig. S16. EIS spectra of symmetric cells assembled with different materials.

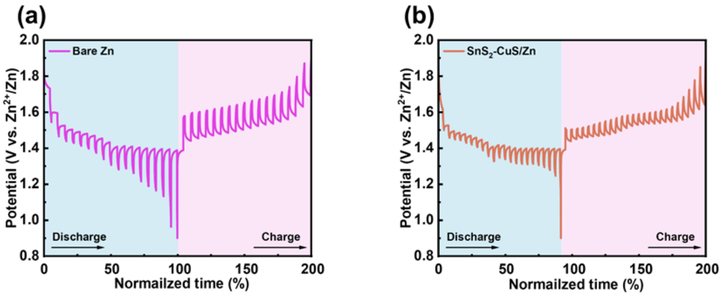

Fig. S17. GITT profiles of full cells with different anodes (a) Bare Zn; (b) SnS_2-CuS/Zn.

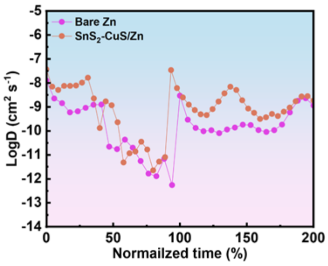

Fig. S18. Zn^{2+} diffusion coefficients.

Table S1. Fitted in-situ EIS data values of CuS battery

Potential (V)	R_s (Ω)	R_{ct} (Ω)	Z_w (Ω)
Initial	1.781	56.21	0.92
0.7	2.042	82.44	1.67
0.5	1.735	50.62	0.56
0.3	1.567	69.34	0.70
0.1	1.512	62.86	0.36
0.3	1.966	70.53	1.70
0.5	1.988	127.5	0.72
0.7	1.622	874.9	2.93
0.9	1.591	658.7	1.04
1	1.391	466.9	1.41

Table S2. Fitted in-situ EIS data values of SnS_2 battery

Potential (V)	R_s (Ω)	R_{ct} (Ω)	Z_w (Ω)
Initial	2.129	100.7	0.95
0.7	2.399	308.5	0.80
0.5	1.552	1209.7	0.59
0.3	1.512	1718.0	0.35
0.1	1.290	282.0	0.09
0.3	3.217	569.8	0.52
0.5	4.093	3407.0	0.43
0.7	4.627	530.5	3.54
0.9	6.641	731.5	0.27
1	9.458	62.73	0.23

Table S3. Fitted in-situ EIS data values of SnS_2-CuS battery

Potential (V)	R_s (Ω)	R_{ct} (Ω)	Z_w (Ω)
Initial	1.26	48.79	0.46
0.7	1.136	69.05	1.54
0.5	1.141	23.2	0.57

0.3	1.118	26.82	0.76
0.1	1.071	39.1	0.43
0.3	1.443	159.5	1.66
0.5	1.275	169.5	1.98
0.7	1.201	649.0	0.63
0.9	1.246	680.5	2.37
1	1.201	240.7	0.28

Table S4. Comparison with other works.

References	Initial specific capacity (mAh g^{-1})	Current density (A g^{-1})	Cycle number	Capacity retention rate	Diffusion coefficients (cm^{-2} s^{-1})
1	53.40	0.5	600	84.3%	10^{-6}～10^{-9}
2	138.00	1.0	1500	58.5%	/
3	46.00	0.5	1000	76.6%	$10^{-9.5}$～$10^{-12.8}$
4	100.00	2.0	170	74.0%	$10^{-12.35}$
5	129.95	0.2	1000	80.8%	10^{-10}～10^{-11}
6	116.00	0.05	100	95.0%	$10^{-9.6}$～$10^{-13.4}$
7	78.41	1.0	1000	82.0%	10^{-11}～10^{-15}
8	55.50	0.5	350	78.8%	10^{-8}～10^{-13}
9	61.5	0.3	90	68.5%	10^{-9}～10^{-15}
This work	102.06	1.0	1000	83.6%	10^{-6}～10^{-10}

Table S5. Comparison of this work with other studies on green chemistry performance.

References	Battery system	Whether metallic electrode materials are required	Electrolyte type	Green benefits
10	Lithium-ion battery	Requirement	1 M $LiPF_6$ in EC: DMC (1:1, v/v)	The system requires metallic lithium as the counter electrode, employs flammable organic electrolytes, and must account for the associated safety and environmental hazards.
11	Lithium-sulfur battery	Requirement	1 M LiTFSI and 1 wt% $LiNO_3$ in DOL/DME (v/v, 1: 1)	Requires lithium metal as the counter electrode. Sulfur as active material is explosive. Flammable organic electrolytes pose serious safety and environmental risks.
12	Sodium-ion battery	Dispensability	1 M $NaClO_4$ dissolved in EC: PC: DMC = 1:1:1 (v/v) with 2 vol% FEC	The mixture of multiple organic electrolytes raises safety and environmental concerns.
13	Zinc-air battery	Requirement	6 M KOH+ 0.2 M $Zn(OAc)_2$	For electrochemical measurements, a Hg/HgO

				reference electrode containing heavy metals is required, together with highly concentrated strong alkaline electrolytes.
14	Zinc-ion battery	Requirement	2 M $ZnSO_4$+0.2 M $MnSO_4$	The zinc metal counter electrode is required. Severe issues including zinc dendrite formation and hydrogen/oxygen evolution at the zinc anode significantly limit the cycle life of the battery.
This work	Rocking-chair zinc-ion battery	Dispensability	2 M $ZnSO_4$	It eliminates the reliance on zinc metal anodes, thereby reducing the over-exploitation and excessive consumption of zinc ore resources. Moreover, low-toxicity aqueous electrolytes are adopted with no flammability risks.

References

1 J. Wei, Q. Kuang, M. Huang, Y. Li, H. Zhou, Q. Fan, Y. Dong, Y. Zhao, *Chem. Eng. J.* 2025, **505**, 159217. https://doi.org/10.1016/j.cej.2025.159217.

2 Q. Lei, J. Zhang, Z. Liang, Y. Yue, Z. Ren, Y. Sun, Z. Yao, J. Li, Y. Zhao, Y. Yin, P. Huai, Z. Lv, J. Li, Z. Jiang, W. Wen, X. Li, X. Zhou, D. Zhu, *Adv. Energy Mater.* 2022,

12, 2200547. https://doi.org/10.1002/aenm.202200547.

3 X. Chen, R. Huang, M. Ding, H. He, F. Wang, S. Yin, *ACS Appl. Mater. Interfaces* 2022, **14**, 3961-3969. https://doi.org/10.1021/acsami.1c18975.

4 C. Lin, G. Suo, J. Li, R. Mu, L. Habib, X. Hou, X. Ye, Y. Yang, *Chem. Eng. J.* 2025, **521**, 166539. https://doi.org/10.1016/j.cej.2025.166539.

5 J. Wu, Q. Kuang, P. Jiang, M. Huang, J. Wei, Q. Fan, Y. Dong, Y. Zhao, *Mater. Today Energy* 2024, **42**, 101505. https://doi.org/10.1016/j.mtener.2024.101505.

6 Y. Cao, Y. Qian, L. Chen, T. Song, Y. Pei, X. Wang, X. Wu, Y. Dong, F. Liu, B. Long, *J. Energy Storage* 2025, **125**, 116986. https://doi.org/10.1016/j.est.2025.116986.

7 S. Chen, Y. Liu, S. Zhang, W. Chen, X. Zhao, Z. Cheng, X. Pan, *J. Energy Storage* 2026, **161**, 121915. https://doi.org/10.1016/j.est.2026.121915.

8 P. Cai, X. He, K. Wang, Z. Zhang, Q. Wang, Y. Liu, H. Li, M. Zhou, W. Wang, K. Jiang, *Carbon Energy* 2025, **7**, e691. https://doi.org/10.1002/cey2.691.

9 K. Sun, Z. Xiao, Y. Shen, H. Lv, J. Zhu, J. Pang, Y. Zheng, W. Kong, L. Chen, *Nano Res.* 2024, **17**, 2781-2789. https://doi.org/10.1007/s12274-023-6207-8.

10 S. Rostami, F. Ghasemipur, J. K. R. Modigunta, P. Ahmadibarshahi, G. Murali, Y. J. Seo, Y. H. Park, S. J. Lee, S. Kheawhom, M. Jourshabani, B.-K. Lee, I. In, *Chem. Eng. J.* 2026, **536**, 175806. https://doi.org/10.1016/j.cej.2026.175806.

11 Y. Li, M. Zhang, Z. Xu, Z. Liu, M. Chuai, X. Xiao, X. Guo, G. Zhou, Y. Mai, F. Xu, H. Li, *Adv. Mater.* 2026, e73073. https://doi.org/10.1002/adma.73073.

12 S. Li, H. Wang, Z. Huang, S.-S. Kim, Z. Long, K. Liu, S. Liu, Q. Zhang, L. Zhang, S. Dai, *Adv. Funct. Mater.* 2026, e75230. https://doi.org/10.1002/adfm.75230.

13 J. Li, S. Kang, H. Zhang, J. Yang, P. Wan, Z. Li, S. Wu, Y. Sun, Q. Yang, *Green Chem.* 2025, **27**, 10755-10766. https://doi.org/10.1039/D5GC02131F.

14 Z. Zhou, J. Tong, J. Guo, S. Guo, S. Liu, Z. Qin, M. Luo, C. Wang, S. Liu, *Green Chem.* 2024, **26**, 6704-6712. https://doi.org/10.1039/D4GC01557F.